Available online at www.sciencedirect.com

SciVerse ScienceDirect

Ceramics International 39 (2013) 6795–6803

CERAMICS INTERNATIONAL

www.elsevier.com/locate/ceramint

Controllable synthesis of $CaTi_2O_4(OH)_2$ nanoflakes by a facile template-free process and its properties

Weixia Dong[a,b], Bin Song[c,*], Gaoling Zhao[a,**], Gaorong Han[a]

[a]State Key Laboratory of Silicon Materials & Department of Materials Science and Engineering, Zhejiang University, Hangzhou 310027, PR China
[b]Department of Materials Science and Engineering, Jingdezhen Ceramic Institute, Jingdezhen 333001, PR China
[c]Department of Physics, Zhejiang University, Hangzhou 310027, PR China

Received 18 January 2013; received in revised form 5 February 2013; accepted 5 February 2013
Available online 13 February 2013

Abstract

Serrated leaf-like $CaTi_2O_4(OH)_2$ nanoflake crystals were synthesized via a template-free and surfactant-free hydrothermal process. The samples were characterized by X-ray diffraction (XRD), field emission scanning electron microscopy (FESEM), transmission electron microscopy (TEM) and high-resolution transmission electron microscopy (HRTEM). The growth process for $CaTi_2O_4(OH)_2$ nanoflakes was dominated by a crystallization–dissolution–recrystallization growth mechanism. BET analysis showed that $CaTi_2O_4(OH)_2$ nanoflakes had mesoporous structure with an average pore size of 8.7 nm, and a large surface area of 88.4 $m^2\,g^{-1}$. Cyclic voltammetry and galvanostatic charge–discharge tests revealed that the electrode synthesized from $CaTi_2O_4(OH)_2$ nanoflakes reached specific capacitances of 162 F g^{-1} at the discharge current of 2 mA cm^{-2}, and also exhibited excellent electrochemical stability. Published by Elsevier Ltd and Techna Group S.r.l.

Keywords: $CaTi_2O_4(OH)_2$; Nanoflakes; Template-free; Specific capacitance; Photocatalytic activity

1. Introduction

Calcium titanium oxides are nontoxic and cheap materials. Traditional calcium titanium oxides, e.g. $CaTiO_3$, which mostly present the cubic or orthorhombic structure, have attracted much interest due to their widespread applications in the electronic, biological, catalytic and optic fields [1–6]. Recently, $CaTi_2O_4(OH)_2$ was obtained during preparation of $CaTiO_3$ [7]. $CaTi_2O_4(OH)_2$ is a layered metal hydroxide [8–10], which is constructed by the periodic stacking of positively charged $(CaTi)(OH)_2$ octahedral layers, balanced by interlayer anions and water molecules that bind the sheets together. Usually, layered metal hydroxides have applications in the fields of catalysts, absorbers, anion exchange, electroactive and photoactive materials [11–13]. As a layer metal hydroxide material, however, $CaTi_2O_4(OH)_2$ is little known, and no study has been reported on its physical and chemical properties. Therefore, it is interesting to study the preparation and properties of $CaTi_2O_4(OH)_2$.

In the present work, $CaTi_2O_4(OH)_2$ serrated leaf-like nanoflake structure was synthesized by a simple hydrothermal process. The growth mechanism of $CaTi_2O_4(OH)_2$ serrated leaf-like nanoflake was studied. Moreover, the photocatalytic and electrochemical properties of $CaTi_2O_4(OH)_2$ nanoflake were investigated.

2. Experimental

2.1. Synthesis

$CaTi_2O_4(OH)_2$ crystals were synthesized in an aqueous medium by a hydrothermal method. Butyl titanate (TBOT, Sigma-Aldrich, 99%) and calcium chloride dihydrate ($CaCl_2\cdot 2H_2O$) were used as starting materials. $CaCl_2\cdot 2H_2O$:TBOT:water:ethanol molar ratio was 1:1:50:10. In a typical synthesis, firstly, ethanol was added dropwise to the solution of TBOT, forming solution A. Secondly, solution A was added to $CaCl_2\cdot 2H_2O$ aqueous solution, forming suspension

*Corresponding author. Tel./fax: 86 571 87951326.
**Corresponding author. Tel./fax: 86 571 87952341.
E-mail addresses: bzsong@css.zju.edu.cn (B. Song), glzhao@zju.edu.cn (G. Zhao).

0272-8842/$ - see front matter Published by Elsevier Ltd and Techna Group S.r.l.
http://dx.doi.org/10.1016/j.ceramint.2013.02.010

B. After suspension B was stirred for 5 min, NaOH was added to suspension B to adjust the pH value to 8. The mixed suspension was kept under vigorous stirring at room temperature. Subsequently, the autoclave was sealed and maintained at 180 °C for 36 h, followed by a natural cooling to room temperature. Afterward, the final products were centrifuged, washed with deionized water and absolute ethanol several times, and finally dried in a vacuum oven at 90 °C for 12 h. In order to investigate the growth mechanism of nanoflakes, the reaction times lasting 3 h, 9 h, 12 h, 18 h, 24 h, 36 h and 48 h were also empolyed, keeping all other experimental parameters constant.

2.2. Sample characterization

Crystal phases of the samples were characterized by X-ray diffraction (XRD, PANalytical X'Pert Pro, Holland), in a 2θ range from 5° to 80°, using Cu-Kα radiation ($\lambda = 0.15420$ nm) operating at 50 kV and 40 mA. Morphologies and compositions of the samples were investigated by field emission scanning electron microscopy (FESEM, Hitachi S-4800, Japan) equipped with an EDS system operating at an accelerating voltage of 5.0 kV or 15 kV (15 kV for EDS). Microstructures of the samples were observed by transmission electron microscopy (TEM) operating at an accelerating voltage of 160 kV, and high-resolution transmission electron microscopy (HRTEM, FEI Tecnai G2 F-30, Holland) operating at an accelerating voltage of 200 kV. Nitrogen adsorption–desorption isotherms were collected at 77 K on a Micromeritics TriStar ii 3020 analyzer. Specific surface areas were estimated by using the Brunauer–Emmett–Teller (BET) method and pore sizes were determined with the Barrett–Joyner–Halenda (BJH) method by using nitrogen branches of isotherms.

2.3. Photocatalysis experiments

$CaTi_2O_4(OH)_2$ powders were used as photocatalysts to degrade methyl orange (MO) in an aqueous suspension with an initial concentration of 10^{-5} M. Firstly, 10 mg of $CaTi_2O_4(OH)_2$ powder samples was seperately put in 10 ml methyl orange (MO) aqueous solution, and was put for 24 h in the dark to establish the adsorption equilibrium. The suspension was then exposed to UV light (254 nm, 11 W). Light irradiation time was 0 h, 0.5 h, 1.0 h, 1.5 h, 2.0 h, 2.5 h and 3 h. The degradation under UV irradiation was subtracted by that of the blank contrast experiment because ultraviolet radiation itself can also decompose MO [14]. The photocatalytic activity was characterized by the photodegradation ratio of A/A_0, because the concentration of methyl orange solution and its absorbance are in direct proportion, where A_0 is the optical absorbance of initial methyl orange aqueous solution at 460 nm, and A is the optical absorbance of methyl orange aqueous solution at 460 nm after degradation.

2.4. Electrochemical characterization

2.4.1. Electrode for electrochemical capacitor

Work electrode samples were prepared from the samples with reaction time of 36 h and 12 h, hereafter named as capacitor electrode (36 h) and capacitor electrode (12 h) respectively. The work electrode was prepared by mixing 80 wt% of above mentioned samples, 10 wt% of acetylene black and 10 wt% of poly(tetrafluoroethylene). The mixture was pressed (8 MPa) onto a nickel grid with a size of $1.5 \times 1.5\ cm^2$. The weight of each electrode was approximately 8.4 mg. Electrochemical measurements were carried out by means of an electrochemical analyzer system, CHI660B (Chenhua, Shanghai, China) in a three-compartment cell with a working electrode, a platinum plate counter electrode and a saturated calomel electrode (SCE) reference electrode. Galvanostatic charge–discharge was carried out by LAND CT2001A test system (Chenhua, Shanghai, China).

2.4.2. Electrode for lithium ion battery.

Coin-type cells were assembled in a glove-box filled with pure argon, using the $CaTi_2O_4(OH)_2$ powder samples with reaction time of 36 h prepared for 36 h assembly as the positive electrode and the lithium metal as the negative electrode. The working electrode was fabricated by compressing a mixture of $CaTi_2O_4(OH)_2$ nanoflake (85%), acetylene black (10%), and poly(tetra-fluoroethylene) (5%) onto an aluminum foil. The electrolyte was 1 M $LiPF_6$ (Merck, battery grade) in a mixture of ethyl carbonate (EC) and dimethyl carbonate (DMC; 1:1 in volume ratio). The charge–discharge measurement was carried out in a Neware battery test system BTS-XWJ-6.83S-2010320 (Newell, Shenzhen, China).

3. Results and discussion

3.1. $2O_4(OH)_2$ structure",5,1,2>Morphological and microstructure of $CaTi_2O_4(OH)_2$ structure

Fig. 1(a) shows FESEM images of the sample synthesized at 180 °C for 36 h. It reveals that the irregular serrated leaf-like nanoflake are obtained. The TEM image (Fig. 1(b)) reveals that the sample exhibits an irregular serrated leaf-like crystals geometry with a sharp tip 10–20 nm in thickness and 200–500 nm in plane size. Fig. 1(c) shows the HRTEM image of the sample. It is found that the spacing of the lattice fringes is about 0.257 nm, corresponding to the (371) plane of $CaTi_2O_4(OH)_2$. The corresponding SAED pattern (inset in Fig. 1(c)) reveals that single crystalline structure is obtained. Further studies of the SAED pattern and HRTEM image demonstrate that the nanoflake grows along the [201] direction (indicated with an arrow). EDS analysis of the selected sample (Fig. 1(d)) also shows that the sample is composed of Ca and Ti with an atomic ratio of about 1:2, which is close to the stoichiometry of $CaTi_2O_4(OH)_2$. Furthermore, XRD

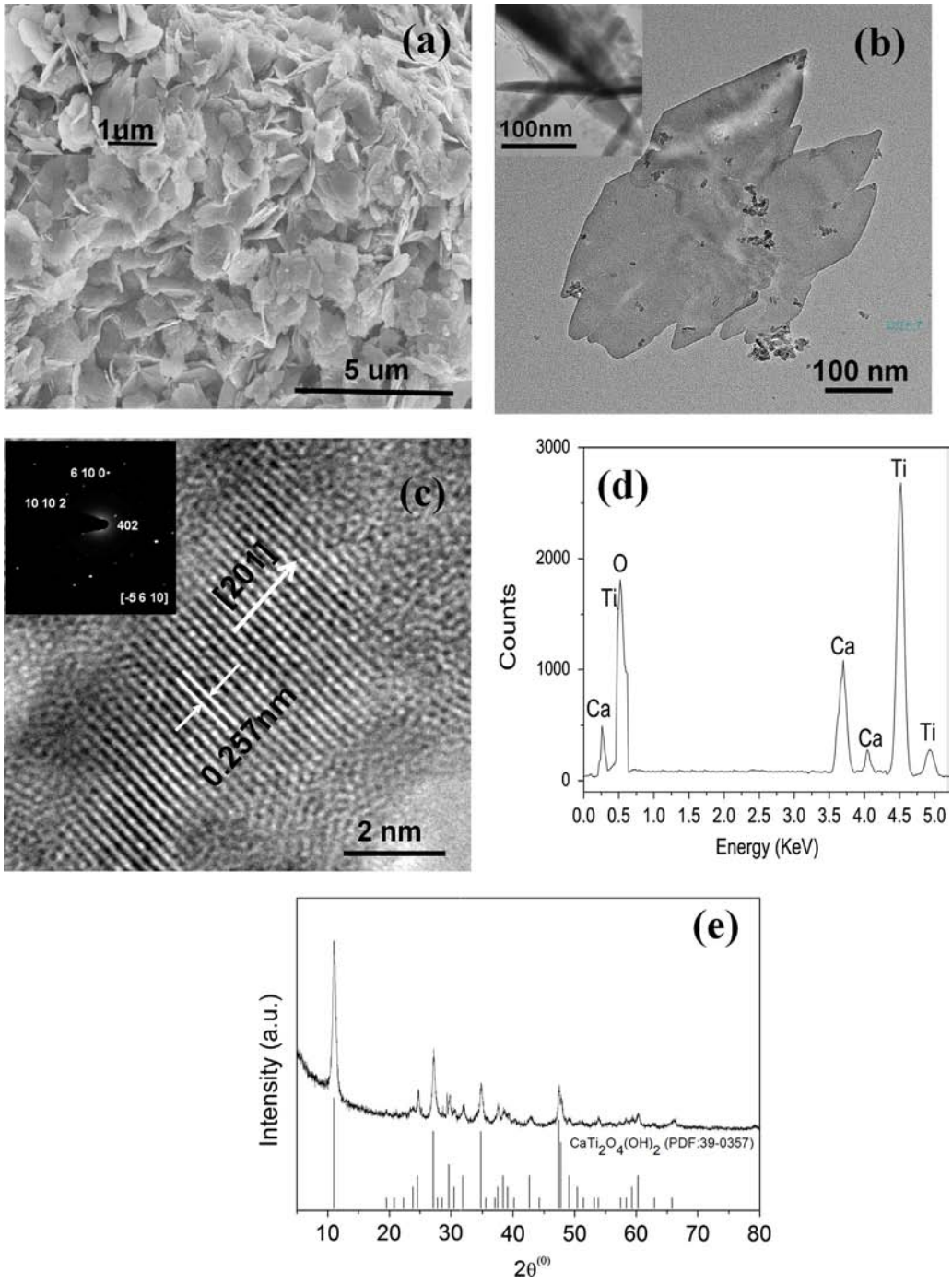

Fig. 1. Microstructure of $CaTi_2O_4(OH)_2$ nanoflake synthesized at 180 °C for 36 h: (a) FESEM images, (b) TEM images, (c) HRTEM images and SAED pattern (inset in (c)), (d) EDS element analysis, and (e) XRD pattern.

pattern of the sample (Fig. 1(e)) also confirms that only $CaTi_2O_4(OH)_2$ (JCPDS card 39-0357) is obtained.

In order to investigate the formation process of nanoflakes, the reaction time was varied and resultant samples were characterized by XRD and SEM. Fig. 2 shows XRD patterns of samples synthesized at 180 °C for various reaction times. When the reaction time is 3 h, that is the initial stage of the hydrothermal reaction, amorphous phase is obtained. When the reaction time is extended to 9 h, a crystalline sample is obtained. The crystal belongs to kassite $CaTi_2O_4(OH)_2$. When the reaction time further increases, peak intensities of $CaTi_2O_4(OH)_2$ strengthen. The crystallinity of samples is estimated from XRD intensity data by using the formula expressed as follows [15,16]:

$$X = \left(I_d / I_t\right) \times 100\%$$

where X is the average of the crystallinity (calculated from XRD curve), I_d is intensity of (040), (031), (151), (251), (331),

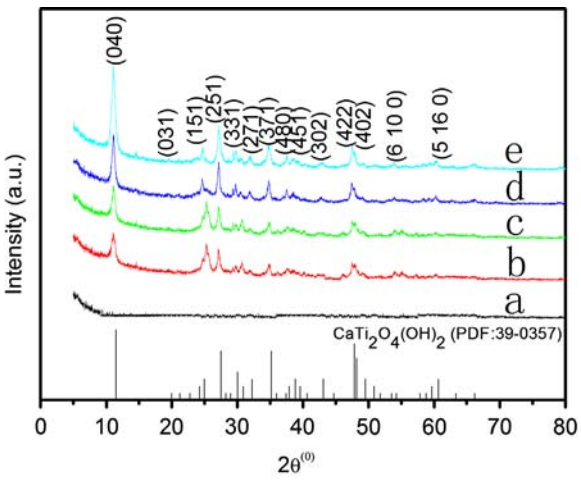

Fig. 2. XRD pattern of samples synthesized at 180 °C for (a) 3 h, (b) 9 h, (c) 12 h, (d) 18 h, and (e) 24 h.

Table 1
Effects of the reaction time on crystallinity, surface area and average pore size of samples.

Time (h)	Crystallinity X (%)	Surface area ($m^2\,g^{-1}$)	Average pore size (nm)
9	64.90	192.4	16.9
12	66.59	242.2	17.6
18	69.57	225.9	15.2
24	78.10	123.1	11.2
36	79.03	88.4	8.7

(271), (371), (480), (451), (302), (402), (422), (6 10 0) and (5 16 0) diffraction peaks, and I_t is the sum of intensities of the sample. The calculated results are listed in Table 1, indicating that the crystallinity (X) increases with increasing reaction time.

Fig. 3 shows corresponding FESEM images of above samples. When the reaction time is 3 h, the sample is irregular aggregated particles (Fig. 3(a)). When the reaction time is 9 h, lots of nanofibers form (Fig. 3(b)). When the reaction time is 12 h, some nanofibers dissolve and transform into small nanoflakes (Fig. 3(c)). When the reaction time extends to 18 h, more and more irregular nanoflakes are obtained and nanofibers disappear (Fig. 3(d)). Extending the reaction time to 24 h, nanoflakes grow further (Fig. 3(e)). Well-defined nanoflakes are obtained for 36 h (Fig. 3(f)). Further extending of the reaction time (48 h) does not change the microstructure obviously.

3.2. Growth mechanism

The growth mechanism of $CaTi_2O_4(OH)_2$ nanoflakes can be explained as follows. At the initial stage of reaction, TBOT hydrolyses and transforms into titanium hydroxide. Titanium hydroxide transforms into titanium dioxide (TiO_2) by dehydrating condensation; then titanium dioxide dissolves and releases Ti^{4+} ions gradually, which depends on the concentration of OH^- [17–19]. Due to low amount of active OH^- at pH = 8, titanium dioxide partly dissolves and releases Ti^{4+} ions in the hydrothermal process. The reaction is controlled by the amount of dissolved Ti^{4+} in the solution, which leads to the formation of small nuclei that grow into $CaTi_2O_4(OH)_2$ crystallites as shown in eq. (1). After nucleation, the nuclei grow by incorporating monomers remaining in the reaction medium. As a subsequent result, $CaTi_2O_4(OH)_2$ is obtained:

$$Ca^{2+} + Ti^{4+} + TiO_2 + 6OH^- \rightarrow CaTi_2O_4(OH)_2 + 2H_2O$$

Three obvious evolution stages can be observed from the microstructure of sample as shown in Fig. 3. Firstly, at an early hydrothermal stage, according to Figs. 2 and 3(a) amorphous particles aggregate. Due to anisotropic crystal structure [20–23], these aggregated amorphous particles grow to low dimensions and result in the formation of many nanofibers (Fig. 3(b)). These nanofibers tend to arrange randomly in order to lower their surface energy. When the reaction time increases, the reaction rate slows down with the decrease of the reactants' concentration. Considering that no additional templates are added in the formation process, based on growth habits of crystals [22], partial $CaTi_2O_4(OH)_2$ nanofibers start to dissolve in the solution and many tiny nanoplates are formed in the recrystallization process (Fig. 3(c) and (d)). This dissolution and recrystallization process is very similar to the recent work reported by Luo et al. [23], which is based on the nanoflake growth of novel flowerlike $BaMoO_4$ nanostructures. When the reaction time is extended to 24 h and 36 h, crystallization of $CaTi_2O_4(OH)_2$ increases dramatically (Fig. 2 and Table 1), and finally forms larger nanoflakes (Fig. 3(f)). Accordingly, a possible growth model for the reaction synthesis is suggested in Fig. 4.

3.3. 2 adsorption–desorption properties",5,1,2>N_2 adsorption–desorption properties

Fig. 5 shows N_2 adsorption–desorption isotherms of samples with various reaction times. All the isotherms of samples are of classical type IV with a distinct hysteresis loop observed in the range of 0.5–1.0P/P_0. All samples show strong N_2 adsorption of nitrogen in the higher pressure region ($P/P_0 > 0.5$), indicating the presence of mesopores [24]. The inset of Fig. 5 shows the pore-size distribution of samples prepared for various reaction times. The average pore size, which is ranged from 5–20 nm, is also listed in Table 1, confirming the mesoporous structure of samples. The mesoporous structure can be possibly attributed to mesoporous stacking of particles. The most external surface of the porous stacking structure is observed from Fig. 3. Results for the surface area, pore volume and pore size of samples are also listed in Table 1. For samples synthesized for 9 h, 12 h and 18 h, surface areas are 192.4, 242.2 and 225.9 $m^2\,g^{-1}$ respectively, which are around 200 $m^2\,g^{-1}$. When reaction time increases to 24 h and 36 h, surface areas are 123.1 and 88.4 $m^2\,g^{-1}$ respectively. Among all samples,

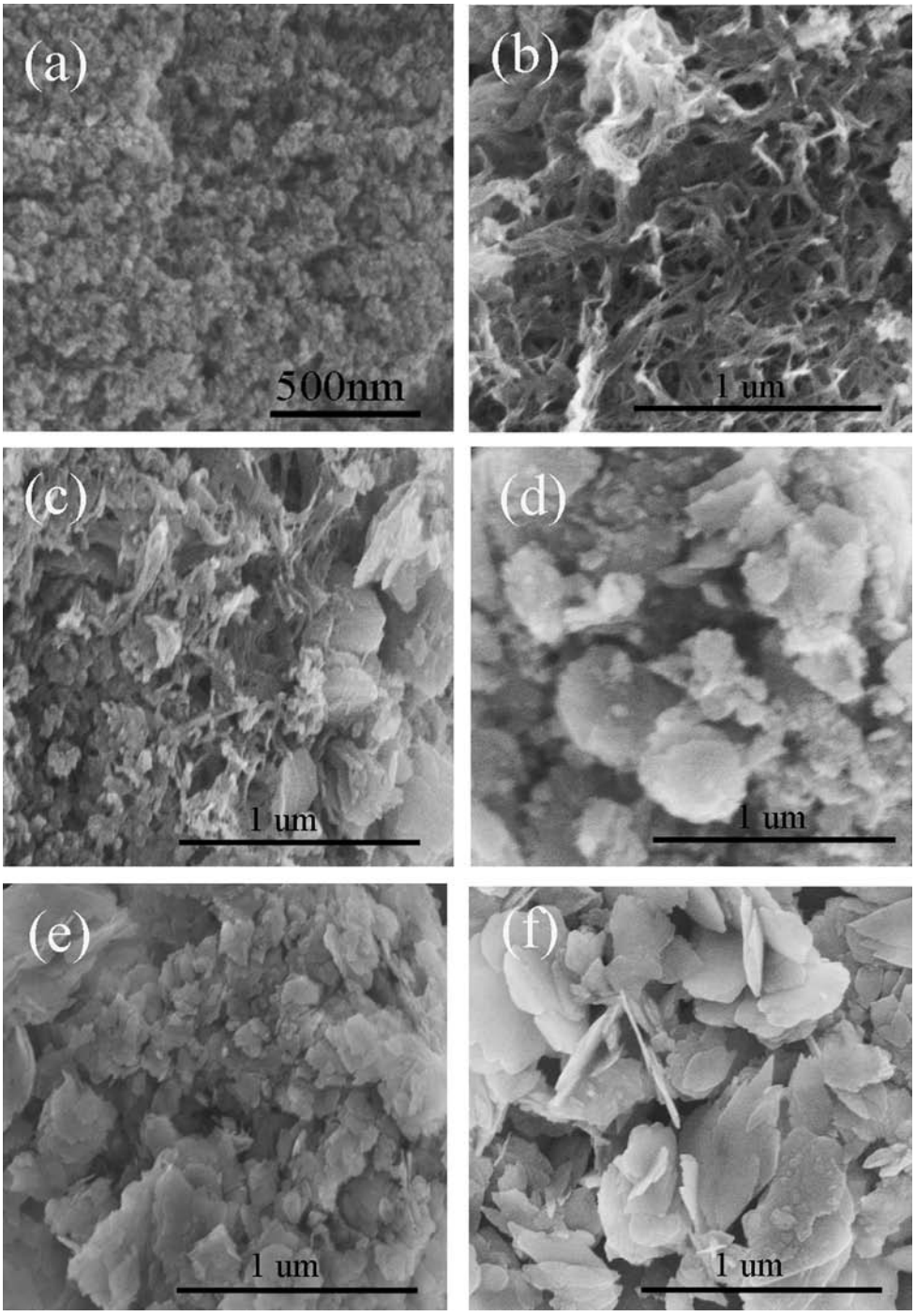

Fig. 3. Typical FESEM images of samples synthesized at 180 °C for (a) 3 h, (b) 9 h, (c) 12 h, (d) 18 h, (e) 24 h, and (f) 36 h.

the sample prepared for 36 h has the smallest surface area. This can be attributed to the enhancement of $CaTi_2O_4(OH)_2$ crystallization and further growth (Table 1 and Fig. 3).

3.4. Photocatalytic properties

Fig. 6 shows the photocatalytic activity of samples for the degradation of MO under UV light irradiation. It can be seen that the photocatalytic activity of samples increases with increasing reaction time. It is surprising that the sample synthesized for 36 h has the highest photodegradion rate of 94.5% in 120 min, although the BET surface area of this sample prepared at 36 h (BET: 88.4 $m^2 g^{-1}$) is lower than that of the others (Table 1). The reaction time affects the photocatalytic activity by controlling the crystallinity, specific surface area, and pore size. It is known that the crystal increase is beneficial to the photocatalytic activity because of the reduction of photogeneration carriers recombination [25]. For crystallinity, when the reaction time increases, the crystallinity increases, which results in the

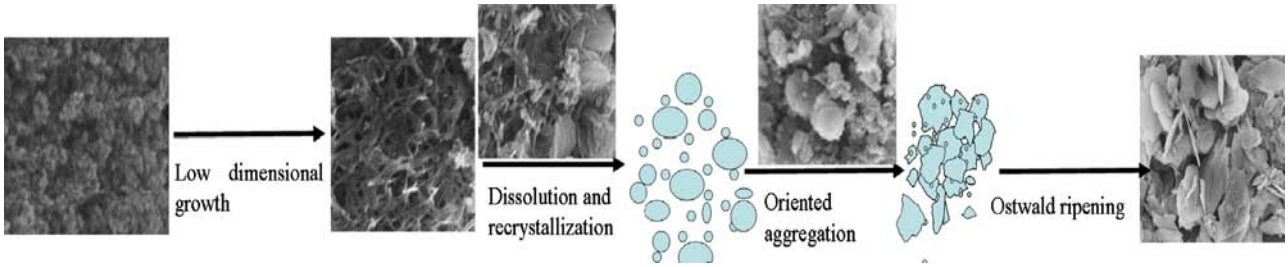

Fig. 4. Schematic illustration of the morphology evolution of serrated leaf-like $CaTi_2O_4(OH)_2$ nanoflake.

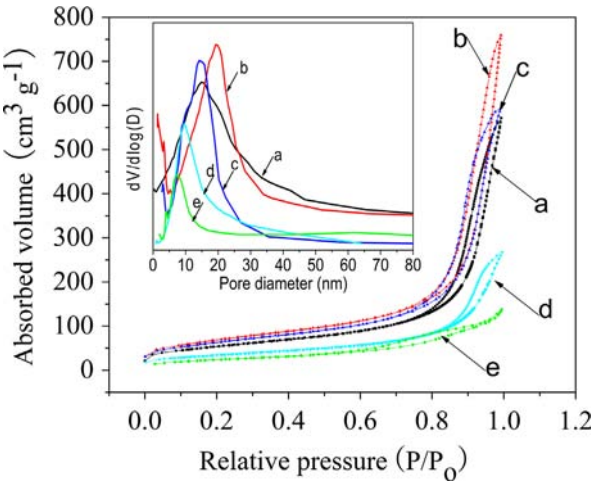

Fig. 5. N_2 adsorption–desorption isotherms and the pore size distribution (inset) of samples synthesized at 180 °C for (a) 9 h, (b) 12 h, (c) 18 h, (d) 24 h, and (e) 36 h.

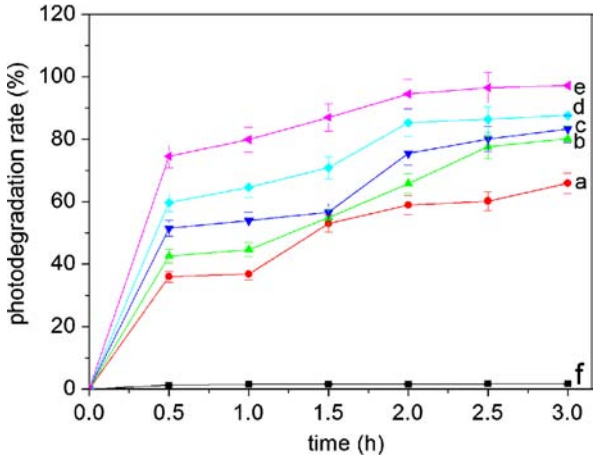

Fig. 6. Photocatalytic activity of samples prepared for various reaction times: (a) 9 h, (b) 12 h, (c) 18 h, (d) 24 h, (e) 36 h and (f) blank (without photocatalyst).

decrease of crystal defects; thus the recombination of photogenerated electrons and holes is inhibited, resulting in the improvement of photocatalytic activity. As the surface area increases, more unsaturated coordination sites are exposed to the reactants, and more MO molecules are effectively adsorbed to the surface of the photocatalysts, and improve the photocatalytic properties [26]. On the other hand, as for the pore size, the decrease of pore size results in closer pore walls, which leads to more adsorption of MO on the active sites of pore walls, and so photocatalysts with the smaller pore sizes decompose substances more readily and effectively [14,27]. Accordingly, when the reaction time is less than or equal to 12 h, the increase of photocatalytic activity can be ascribed to the enhancement of crystallinity and increase of the specific surface area with increasing time (Table 1 and Fig. 5). When the reaction time is 18 h, the specific surface area remains almost the same as that of the sample of 12 h. On the other hand, the crystallinity further increases (Fig. 2). Therefore, the photocatalytic activity increases. As for the samples that are hydrothermally synthesized for 24 h and 36 h, specific surface areas decrease to 123.1 and 88.4 $m^2\,g^{-1}$ (Table 1 and Fig. 5), respectively. However, the crystallinity increases and pore size decreases dramatically (Table 1 and Fig. 2). In addition, the nanoflake structure is obtained (Fig. 3(e) and (f)). Nanoflake has a developed surface, and thus many of their active sites are accessible for MO molecules [28,29]. On the other hand, it is commonly accepted that a larger band gap corresponds to a more powerful redox ability [15]. The increase in band gap with time results in an enhanced oxidation–reduction potential (see Supporting information Fig. S1). Therefore, 24 h and 36 h samples provide much higher photocatalytic activity than that of samples with shorter reaction time.

3.5. Electrochemical properties

As a double-layered hydroxide, one of the most important applications is in capacitors [30–33]. Fig. 7 shows electrochemical properties of $CaTi_2O_4(OH)_2$ capacitor electrode. Fig. 7(a) shows cyclic voltammetry (CV) curves of $CaTi_2O_4(OH)_2$ capacitor electrode (36 h) and capacitor electrode (12 h). Obviously, the area surrounded by curve m is larger than that of curve n. Because the capacitance is directly proportional to the area surrounded by CV curves [34], it can be suggested that the capacitor electrode (36 h) has a larger specific capacitance value than that of capacitor electrode (12 h). Furthermore, the curve shape reveals that the capacitance characteristic of $CaTi_2O_4(OH)_2$ is different from that of the electrical double-layer capacitance, which produces a CV curve close to an ideal rectangular shape [35]. A pair of redox peaks is observed in CV curves (Fig. 7(a)), which

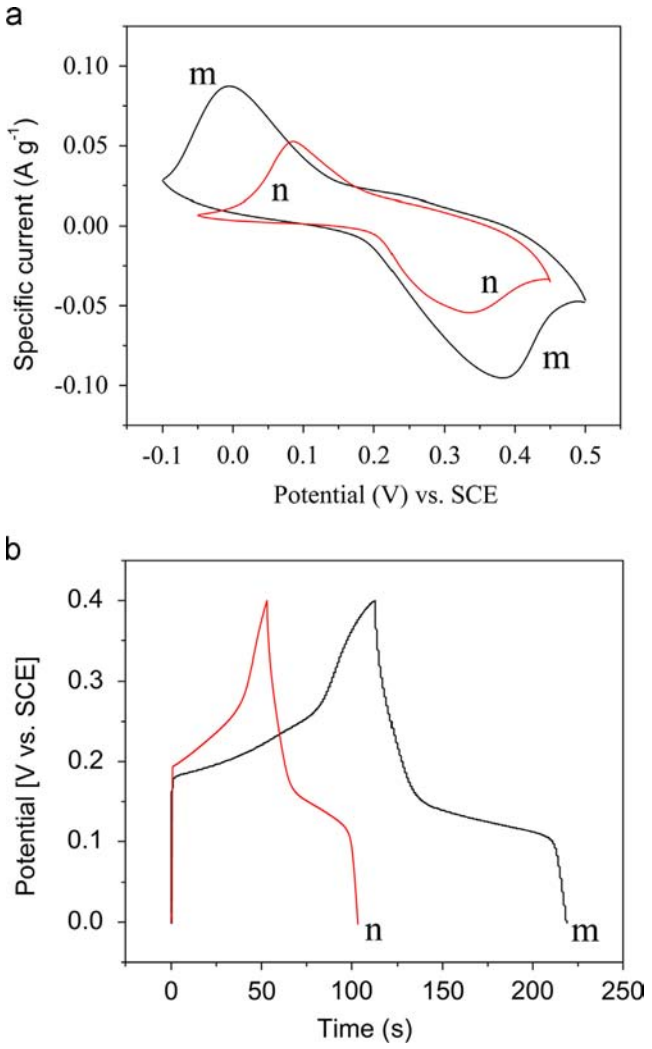

Fig. 7. (a) Cyclic voltammogram (CV) curves of the synthesized $CaTi_2O_4(OH)_2$ (LDH-Ti(IV)) capacitor electrodes synthesized from the samples prepared for 36 h (curve m) and 12 h (curve n) within the potential range of 0–0.4 V (vs. SCE) at a scan rate of 30 mV s^{-1} in 6 M aqueous KOH electrolyte. (b) First six charge–discharge cycles of $CaTi_2O_4(OH)_2$ nanoflake electrode in 6 M KOH within a potential window of 0–0.4 V vs. SCE at a charge–discharge current of 2 mA cm^{-2}.

correspond to the reaction Ti(IV)↔Ti(III). According to literatures [36,37], it is considered that OH^- ions replace interlayer anions rapidly as soon as the electrode is immersed into KOH solution, thus the redox reaction may occur as in eq. (2). The galvanostatic charge–discharge test is especially valuable to study redox electrochemical capacitors. Fig. 7(b) shows charge–discharge curves of $CaTi_2O_4(OH)_2$ capacitor electrodes which are measured in the potential range of 0–0.4 V at the discharge current of 2 mA cm^{-2}. By using the data of Fig. 7(b), specific capacitances were calculated based on the equation $C=(I\,\Delta t)/(m\,\Delta v)$, where I is the charge or discharge current (A), m is the mass of active material in the electrode (mg), Δv is the voltage difference between the upper and lower potential limits (V), Δt is the charge or discharge time (s), and C is specific capacitance (F g^{-1}). The result shows that specific capacitances of $CaTi_2O_4(OH)_2$ capacitor electrode (36 h) and capacitor electrode (12 h) are 162 F g^{-1} and 64 F g^{-1}, respectively. The electrochemical stability of the capacitor electrode (36 h) in 6 M KOH was examined by chronopotentiometry at 6 mA cm^{-2}. The result showed about 5% loss of capacitance after 10,000 consecutive cycles, implying that $CaTi_2O_4(OH)_2$ capacitor electrode had a long-term electrochemical stability. Although the 36 h sample has smaller surface area than that of the 12 h sample the capacitor electrode (36 h) exhibits higher electrochemical characteristics and cycling stability than those of the capacitor electrode (12 h). This can be ascribed to the higher crystallinity of the 36 h sample. On the other hand, as revealed in Table 1, $CaTi_2O_4(OH)_2$ nanoflakes (36 h) have mesoporous structure with an average pore size of 8.7 nm, which will enhance the electrolyte penetration to the inner region of $CaTi_2O_4(OH)_2$ and shorten diffusion paths for both electrodes and conductive ions. In addition, it can also accommodate the strain induced by the volume change during the electrochemical reaction. In a word, $CaTi_2O_4(OH)_2$ capacitor electrode achieves a good cycle ability and high specific capacitance, making it potentially useful for high performance capacitor materials.

$$\text{LDH-Ti(IV)} + OH^-(\text{solution}) \leftrightarrow \text{LDH}(OH^-)\text{–Ti(III)} + e^- \quad (2)$$

3.6. $2O_4(OH)_2$ nanoflake in a lithium ion battery",5,1,2>Performance of $CaTi_2O_4(OH)_2$ nanoflake in a lithium ion battery

Fig. 8 shows electrochemical curves of electrode for lithium ion battery synthesized from $CaTi_2O_4(OH)_2$ nanoflakes with the reaction time of 36 h. Fig. 8(a) shows 1st, 2nd, 10th, and 30th cycles of the $CaTi_2O_4(OH)_2$ electrode for lithium ion battery. Fig. 8(b) shows that the first discharge specific capacity is 244 mA h g^{-1}. The discharge capacity of $CaTi_2O_4(OH)_2$ electrode is 128 mA h g^{-1} after 10 cycles and the discharge capacity remains 112 mA h g^{-1} after 30 cycles. $CaTi_2O_4(OH)_2$ electrode presents a high specific capacity in the first several cycles. This phenomenon can be explained as follows: the large surface area (BET: 88.4 m^2 g^{-1}) results in large electrode–electrolyte contact area. Moreover, small pore sizes (8.7 nm) increase short diffusion paths both for electrons and lithium ions [38,39]. However, the cycling capacity decreases steeply at the initial stage probably because of the Ti(IV)↔Ti(III) transformation in $CaTi_2O_4(OH)_2$ electrode. Investigations of this issue are under way in our laboratory.

4. Conclusions

A single-step, template-free process has been developed to prepare $CaTi_2O_4(OH)_2$ nanoflakes. $CaTi_2O_4(OH)_2$ nanoflakes have been obtained by the hydrothermal method at 180 °C for 36 h. The $CaTi_2O_4(OH)_2$ nanoflakes showed higher photocatalytic activity than that of $CaTi_2O_4(OH)_2$ with various morphologies. Also, $CaTi_2O_4(OH)_2$ capacitor electrode (36 h)

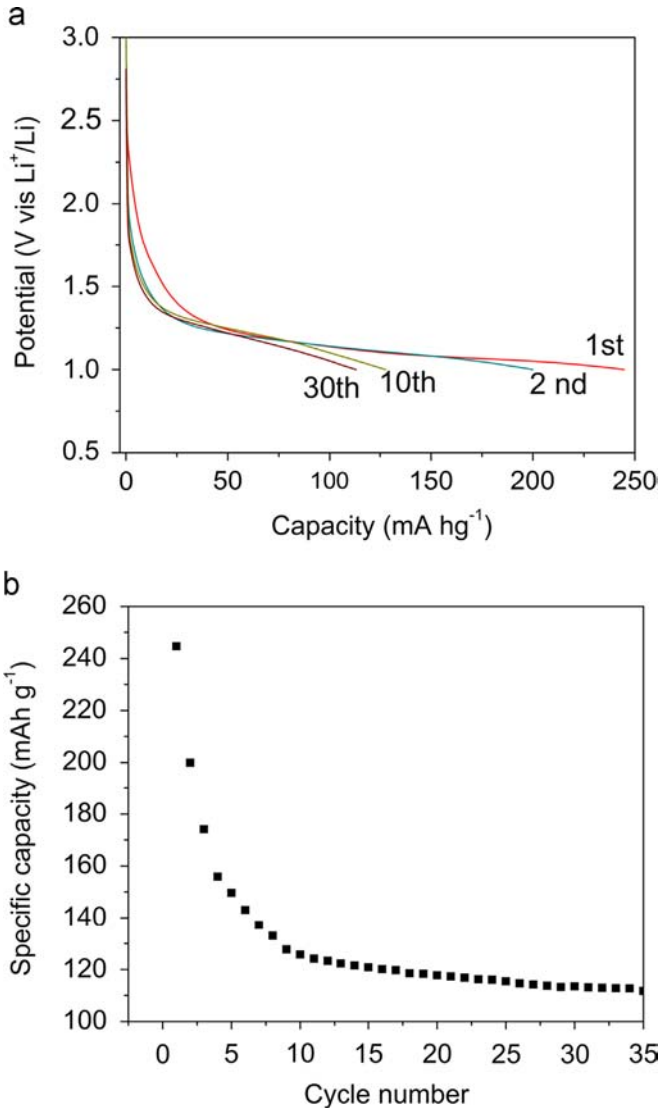

Fig. 8. Electrochemical curves of the $CaTi_2O_4(OH)_2$ nanoflake electrode: (a) discharge/charge curves on the 1st, 2nd,10th, and 30th cycles and (b) discharge capacity vs. cycle number in the voltage range of 0.5–3.0 V with a discharge rate 0.1 C at room temperature.

had a relatively high specific capacitance of 162 F g^{-1} at the discharge current of 2 mA cm^{-2}, and approximately 5% loss of capacitance after 10,000 consecutive cycles, indicating the excellent electrochemical stability of the material. Moreover, it was found that $CaTi_2O_4(OH)_2$ nanoflakes exhibited a certain electrochemical characterization in lithium ion battery.

Acknowledgment

The present work was supported by the National Natural Science Foundation (Grant no. 51172201), National "Twelfth Five-Year" Plan for Science and Technology (2011BAE14B02), Zhejiang Province Key Science and Technology Innovation Team, and New Battery material and Application Science and Technology Innovation Team supports (2010R50013).

Appendix A. Supporting information

Supplementary data associated with this article can be found in the online version at http://dx.doi.org/10.1016/j.ceramint.2013.02.010.

References

[1] T. Liu, X. Zhao, W. Chen, A/B site modified $CaTiO_3$ dielectric ceramics for microwave application, Journal of the American Ceramic Society 89 (2006) 1153–1155.
[2] M. Inoue, A.P. Rodriguez, T. Takagi, N. Katase, M. Kubota, N. Nagai, H. Nagatsuka, N. Nagaoka, S. Takagi, K. Suzuki, Effect of a new titanium coating material ($CaTiO_3$-aC) prepared by thermal decomposition method on osteoblastic cell response, Journal of Biomaterials Applications 24 (2010) 657–672.
[3] T.J. Webster, C. Ergun, R.H. Doremus, W.A. Lanford, Increased osteoblast adhesion on titanium-coated hydroxylapatite that forms $CaTiO_3$, Journal of Biomedical Materials Research A 67 (2003) 975.
[4] N. Sayad, A. Saadi, S. Nemouchi, A. Taibi–Benziada, C. Rabia, Hydrogenation/hydrogenolysis of benzaldehyde over $CaTiO_3$ based catalysts, Studies in Surface Science and Catalysis 175 (2010) 377–380.
[5] L.S. Cavalcante, V.S. Marques, J.C. Sczancoski, M.T. Escote, M.R. Joya, J.A. Varela, M.R.M.C. Santos, P.S. Pizani, E. Longo, Synthesis, structural refinement and optical behavior of $CaTiO_3$ powders: a comparative study of processing in different furnaces, Chemical Engineering Journal 143 (2008) 299–307.
[6] J. Li, Y.C. Zhang, T.X. Wang, M. Zhang, Low temperature synthesis and optical properties of $CaTiO_3$ nanoparticles from $Ca(NO_3)_2 \cdot 4H_2O$ and TiO_2 nanocrystals, Materials Letters 11 (2011) 1556–1558.
[7] Y.J. Huang, M.C. Tsai, H.T. Chiu, H.S. Sheu, C.Y. Lee, Artificial synthesis of platelet-like kassite and its transformation to $CaTiO_3$, Crystal Growth and Design 10 (2010) 1221–1225.
[8] G.S. Peter, R.B. Peter, Structure model for kassite, $CaTi_2O_4(OH)_2$, American Mineralogist 76 (1991) 283–287.
[9] I.E. Grey, W.G. Mumme, I.V. Pekov, D.Y. Pushcharovsky, The crystal structure of chromian kassite from the Saranovskoye deposit, Northern Urals, Russia, American Mineralogist 88 (2003) 1331–1335.
[10] T.E. Howard, J.D. Edward, M. Charles, The problem of cafetite and kassite, American Mineralogist 71 (1986) 1045–1048.
[11] M.P. Agnieszka, V.G. Cathie, F. Elzbieta, Carbon/layered double hydroxide (LDH) composites for supercapacitor application, Energy Fuels 24 (2010) 3346–3351.
[12] H.L. Kang, M. Leoni, H.M. He, G.L. Huang, X.J. Yang, Well-crystallized CO_3^{2-}-type LiAl–LDH from urea hydrolysis of an aqueous chloride solution, European Journal of Inorganic Chemistry 24 (2012) 3859–3865.
[13] W. Shi, Y. Lin, X. Kong, S. Zhang, Y. Jia, M. Wei, D.G. Evans, X. Duan, Fabrication of pyrenetetrasulfonate/layered double hydroxide ultrathin films and their application in fluorescence chemosensors, Journal of Materials Chemistry 21 (2011) 6088.
[14] H. Li, G.L. Zhao, Z.J. Chen, B. Song, G.R. Han, TiO_2–Ag nanocomposites by low-temperature sol–gel processing, Journal of the American Ceramic Society 93 (2010) 445–449.
[15] C.S. Mei, P.Y. Wen, Z.C. Liu, H.X. Liu, Y.D. Wang, W.M. Yang, Z.K. Xie, W.M. Hua, Z. Gao, Selective production of propylene from methanol: mesoporosity development in high silica HZSM-5, Journal of Catalysis 258 (2008) 243–249.
[16] G.M. Sheldrick, Phase annealing in SHELX-90: direct methods for larger structures, Acta Crystallographica A 46 (1990) 467.
[17] Z. Chen, G. Zhao, H. Li, G. Han, B. Song, Effects of water amount and pH on the crystal behavior of a TiO_2 nanocrystalline derived

from a sol–gel process at a low temperature, Journal of the American Ceramic Society 92 (2009) 1024–1029.
[18] W.X. Dong, G.L. Zhao, B. Song, X. Gang, J. Zhou, G.R. Han, Surfactant-free fabrication of $CaTiO_3$ butterfly-like dendrite via a simple one-step hydrothermal route, CrystEngComm 14 (2012) 6990–6997.
[19] Y.J. Huang, H.T. Chiu, C.Y. Lee, Growth of $CaTiO_3$ dendrites and rectangular prisms through a wet chemical method, CrystEngComm 11 (2009) 1904–1909.
[20] C. Pacholski, A. Kornowski, H. Weller, Self-assembly of ZnO from nanodots to nanorods, Angewandte Chemie International Edition 41 (2002) 1188.
[21] W.G. Lu, P.X. Gao, W. Bin Jian, Z.L. Wang, J.Y. Fang, Perfect orientation ordered in-situ one-dimensional self-assembly of Mn-doped PbSe nanocrystals, Journal of the American Chemical Society 126 (2004) 14816–14821.
[22] Z. Tang, N.A. Kotov, M. Giersig, Spontaneous organization of single CdTe nanoparticles into luminescent nanowires, Science 297 (2002) 237.
[23] Y.S. Luo, W.D. Zhang, X.J. Dai, Y. Yang, S.Y. Fu, Facile synthesis and luminescent properties of novel flowerlike $BaMoO_4$ nanostructures by a simple hydrothermal route, Journal of Physical Chemistry C 113 (2009) 4856–4861.
[24] F. Rouquerol, J. Rouquerol, K. Sing, Adsorption by Powders and Porous Solids: Principles, Methodology and Applications, Academic Press, San Diego, 1999.
[25] M.R. Hoffmann, S.T. Martin, W. Choi, W.D. Bahnemannt, Environmental applications of semiconductor photocatalysis, Chemical Reviews 95 (1995) 69.
[26] J. Tang, Z. Zou, J. Ye, Efficient photocatalytic decomposition of organic contaminants over $CaBi_2O_4$ under visible-light irradiation, Angewandte Chemie International Edition 43 (2004) 4463.
[27] L. Gao, Q.H. Zhang, Effects of amorphous contents and particle size on the photocatalytic properties of TiO_2 nanoparticles, Scripta Materialia 44 (2001) 1195–1198.
[28] M.F. Shao, J.B. Han, M. Wei, G. Evans, X. Duan, The synthesis of hierarchical Zn–Ti layered double hydroxide for efficient visible-light photocatalysis, Chemical Engineering Journal 168 (2011) 519–524.
[29] J. Zhang, X. Liu, S. Gao, B. Huang, Y. Dai, Y. Xu, L. Grabstanowicz, T. Xu, From AgI/TiO_2 to Ag/TiO_2: effects of the annealing temperature on the compositions, porous nanostructures, and visible-light photocatalytic properties, Ceramics International 2 (2013) 1011–1019.
[30] Q. Wang, D. O'Hare, Recent advances in the synthesis and application of layered double hydroxide (LDH) nanosheets, Chemical Reviews 112 (2012) 4124–4155.
[31] J. Wang, Z.H. Liu, X. Liu, K. Ooi, Preparation and structural evolution of SiO_2–TiO_2 pillared layered manganese oxide nanocomposite upon intercalating reaction, Journal of Colloidal and Interface Science 307 (2007) 524–530.
[32] Y. He, Q. Liu, T. Mann, P.P. Yang, M.L. Zhang, L.H. Liu, Graphene nanosheet/Ni^{2+}/Al^{3+} layered double-hydroxide composite as a novel electrode for a supercapacitor, Chemistry of Materials 23 (2011) 3509–3516.
[33] L. Wang, D. Wang, X.Y. Dong, Z.J. Zhang, X.F. Pei, X.J. Chen, B. Chen, J. Jin, Layered assembly of graphene oxide and Co–Al layered double hydroxide nanosheets as electrode materials for supercapacitors, Chemical Communications 47 (2011) 3556–3558.
[34] B.E. Conway, Electrochemical Supercapacitors Scientific Fundamental and Technological Applications, Plenum, New York, 1999.
[35] K.R. Prasad, N. Miura, Electrochemically synthesized MnO_2-based mixed oxides for high performance redox supercapacitors, Electrochemistry Communications 6 (2004) 1004–1008.
[36] L.H. Su, X.G. Zhang, Y.J. Liu, Electrochemical performance of Co–Al layered double hydroxide nanosheets mixed with multiwall carbon nanotubes, Solid State Electrochemistry 12 (2008) 1129.
[37] E. Scavetta, M. Berrettoni, F. Nobili, D. Tonelli, Electrochemical characterisation of electrodes modified with a Co/Al hydrotalcite-like compound, Electrochimca Acta 50 (2005) 3305.
[38] Y.Y. Hu, X.T. Huang, K. Wang, J.P. Liu, R.M. Ding, X. Li, Kirkendall-effect-based growth of dendrite-shaped CuO hollow micro/nanostructures for lithium-ion battery anodes, Journal of Solid State Chemistry 183 (2010) 662–667.
[39] H.Y. Wang, T. Abe, S.H. Maruyama, Y. Iriyama, Z. Ogumi, K. Yoshikawa, Graphitized carbon nanobeads with an onion texture as a lithium-ion battery negative electrode for high-rate use, Advanced Materials 17 (2005) 2857–2860.